International Journal of Heat and Mass Transfer 116 (2018) 314–328

Contents lists available at ScienceDirect

International Journal of Heat and Mass Transfer

journal homepage: www.elsevier.com/locate/ijhmt

Reflection and refraction of a thermal wave at an ideal interface

Ben-Dian Nie, Bing-Yang Cao *

Key Laboratory for Thermal Science and Power Engineering of Ministry of Education, Department of Engineering Mechanics, Tsinghua University, Beijing 100084, China

ARTICLE INFO

Article history:
Received 15 July 2017
Received in revised form 8 September 2017
Accepted 11 September 2017

Keywords:
Thermal wave
Reflection and refraction
Ideal interface
Energy distribution
Alternative direction implicit method

ABSTRACT

Thermal waves are of great significance as non-Fourier effects arise with ultrafast heating rates and small system length. This study analytically and numerically investigated the behavior of thermal waves based on the Cattaneo-Vernotte model at an ideal interface. A stable, fast algorithm based on the alternative direction implicit method is introduced to solve the two-dimensional heat conduction problem. When thermal waves meet with an ideal interface, some energy is reflected back while the rest is conveyed across the interface, which are called the reflection and refraction of thermal waves. The changes of the profile and direction and the energy distribution between the reflection and refraction of the thermal waves are studied both analytically and numerically. Regardless of the boundary conditions imposed on the interface, the reflection angle is always identical to the incident angle, and the ratio of the sine of the refraction angle of the thermal waves to that of the incident angle is equal to the ratio of the thermal wave speeds in the two material layers. A theoretical equation to describe the relationships between the energy distribution and the material thermal properties shows that the thermal wave speeds in the materials, the specific heat and the incident angle determine the thermal energy transmittance ratio. Total reflection can occur for some conditions, and the nature of the energy conveyed by thermal waves is interesting and instructive.

1. Introduction

The thermal wave concept originates from the breakdown of the classical Fourier's law of heat conduction which implies an infinite propagation speed of a thermal perturbation [1,2]. Moreover, investigations of the second sound experimentally reveal that heat pulses propagate at finite speed with wave characteristics [3]. In particular, in nanomaterials pure diffusion predicted by Fourier's law fails to describe the heat conduction processes while lots of phonons are transported in the ballistic regime [4]. With the development of ultra-short pulse lasers and the miniaturization of electronic devices, thermal wave propagation in multilayered composite materials is of much significance as non-Fourier effects arise with these ultrafast heating rates and high heat fluxes. The wavelike behavior of thermal waves is widely recognized in biomedical sciences [5–8], microelectronics [9,10], nanomaterials [11–13], semiconductor materials [14–19] and other fields.

Several models have been proposed to characterize the propagation of thermal waves [20–27]. One of the thoughts is to consider that the diffusion coefficient is dependent on temperature and the thermal conductivity is zero in undisturbed medium to give a finite propagation speed [21]. Cattaneo-Vernotte model (CV) was proposed for the starting problem of gas based on kinetic theory [22,23]. Dual-phase-lag model (DPL) considers the relaxation terms for both heat flux and temperature gradient [24]. Phonon hydrodynamic model was proposed based on the solutions for the linear phonon Boltzmann equation [25,26]. Thermomass model (TM) describes the movement of thermomass based on the relation between energy and mass [27]. These models involve the inertia term, nonlocal term and nonlinear term, which could remove the paradox of the infinite heat perturbation speed in Fourier's law. However, the relaxation term of heat flux is thought to be the main factor to make it wavelike. In addition, several models would behave like CV model if given proper parameters. CV model is written as

$$q + \tau \frac{\partial q}{\partial t} = -k\nabla T, \tag{1}$$

where q is the heat flux, T is the temperature, k is the thermal conductivity and τ is the relaxation time. It is simple and typical to study the relaxation effect of thermal waves.

The propagation characteristics of thermal waves have been studied both experimentally and theoretically. Peshkov first measured the second sound velocity in helium II and obtained a speed of 19 m/s at 1.4 K [3]. More evidence of thermal waves was then

* Corresponding author.
E-mail address: caoby@tsinghua.edu.cn (B.-Y. Cao).

http://dx.doi.org/10.1016/j.ijheatmasstransfer.2017.09.043
0017-9310/

Nomenclature

q	heat flux
x	x-coordinate of the domain
y	y-coordinate of the domain
L	length of the domain
t	time
t_0	duration time of imposed pulse
Δx	spatial steps
Δt	time steps
k	thermal conductivity
ρ	density
C_v	specific heat
A	amplitude of imposed pulse
Z	dimensionless relaxation time
T	temperature, period length
B	coefficient matrix
L	upper triangular matrix
U	lower triangular matrix
w	transitional vector
v	speed of thermal wave
r	thermal energy transmittance ratio
m	material speed ratio
G	integral of energy
ΔT_{theory}	temperature rise defined by heat flux
I_{heat}	thermal energy density
a	coefficient of Fourier decomposition
b	coefficient of Fourier decomposition

Greek symbols

τ	total energy
λ	coefficient of analytical solution
α	incident angle, thermal diffusivity
β	refraction angle
θ	reflection angle
ω	frequency of thermal waves
Δ	fluctuation of quantity

Superscripts

$*$	dimensionless parameter
n	time layer

Subscripts

0	reference state
1	materials in the left of interface
2	materials in the right of interface
ini	initial state
diff	diffusion process
ballistic	ballistic process
x	vectors in x-coordinate direction
y	vectors in y-coordinate direction
i	incident process
r	reflection process
t	refraction process
time	in time
space	in space
total	total energy
n	coefficient number
critical	critical value for total reflection
min	minimum value

found in other media, such as solid helium [28,29], NaF [30] and Bi [31]. Tsai and MacDonald [32] performed molecular dynamics (MD) simulations which showed thermal waves can be observed at room temperature or at even higher temperatures within tiny length and time scales. Lee et al. [12] performed first principle calculations and demonstrated that in hydrodynamic phonon transport processes, where R-scatterings can be neglected and momentum is conserved, the second sound phenomenon occurs. Yao et al. [11] used nonequilibrium MD simulations to study heat pulse propagation through graphene and found that thermal waves are transported in a ballistic way. Hua et al. [33] and Tang et al. [4,34,35] developed the phonon Monte Carlo (MC) methods for ballistic-diffusive thermal transport and studied ballistic thermal waves in a thin film.

As in light and sound, the wavelike characteristics of thermal waves are fascinating. The phenomena, such as overshooting [36,37], diffraction [38,39], reflection [40–47], refraction [48] and dispersion [49], have been investigated in detail. In particular, the behaviors of thermal waves at an interface have been studied for its importance in multilayered composite material heat conduction [5,9,50–59]. Tzou [48] used a harmonic analysis to study the reflection and refraction patterns of thermal waves from a surface and at an interface between dissimilar materials to show that the reflection angle depends on the ratio of the thermal wave speeds in both media. Bertolotti [15,40] used a mirage technique to experimentally demonstrate that Snell's law still fits the situation, indicating that the relationships between the angles and material properties still hold. Khadrawi et al. [60] studied the thermal behaviors of perfect and imperfect contact composite slabs using the hyperbolic heat conduction model. Lor and Chu [61,62] emphasized the significant influence of the thermal interface resistance, and extended numerical calculations to two-dimensional planes, in a study of reflected waves from insulated boundaries in a rectangular plate. Ho et al. [50] used the lattice Boltzmann method to investigate the heat transfer in multilayered materials within the framework of the dual-phase-lag (DPL) heat conduction model to show the temperature profiles after a heat pulse passed across an interface. Liu [63] analyzed metal films using the hyperbolic microscopic two-step model and found that the hyperbolic nature of heat in an electron gas significantly affects the thermal behaviors at early times. Al-Nimr et al. [9,53,54] investigated the DPL model for composite structures and considered the influence of the thermal boundary resistance, initial temperature, and material thermal properties on the thermal waves penetrating into another media.

Nevertheless, there are still few theories for the thermal energy distribution when heat pulses propagate through an interface. Previous studies have mainly focused on qualitative descriptions of the temperature profiles, with few discussions about the quantitative characteristics, which are important for precise thermal control in terms of thermal waves. In addition, the increases of system complexities require two-dimensional models to show how the heat propagates in complex structures and whether the principles drawn from one-dimensional assumptions are still applicable.

Interfacial thermal resistance, which is influenced by the properties of materials in contact, can largely affect the profiles of waves and energy transmittance ratio [54]. Hua and Cao [64,65] found that phonons in ballistic-diffusive regime generate boundary temperature jump because of the interactions between phonons

and boundaries, which would increase the interfacial thermal resistance. A radiant boundary condition is the common approach to model the interfacial thermal resistance [66]. However, when the problem is extended from 1D to 2D, more assumptions are necessary except energy conservation and it requires further investigations to understand the thermal behaviors at the interface. Lor and Chu [62] found when the thermal contact resistance is beyond the critical number, a perfect contact assumption could work. In this paper, in order to show the most typical phenomena in the reflection and refraction processes, the interfacial thermal resistance has been ignored.

The objective of this study is to quantitatively analyze the thermal energy distribution at the interface between dissimilar layers with perfect contact, when one side of a rectangular zone is exposed to a time-dependent, pulsed boundary heat flux based on CV model. Section 2 describes the traveling wave method and analyzes the behaviors of thermal waves at an ideal interface. Section 3 introduces a numerical algorithm for this two-dimensional heat conduction problem, based on alternative direction implicit method (ADI). The comparisons in Section 4 between analytical solutions and simulation results show great correspondence. An equation set describing the relationships of angles and energy distribution is proposed. It shows that the incident angle, volumetric heat capacity and thermal wave speed in materials determine the ballistic thermal energy transmittance ratio. The phenomenon of total reflection is observed.

2. Theoretical models

The traveling wave method was used to analyze the thermal wave behaviors at an ideal interface [40]. Regardless of the influence of diffusion term, the thermal wave interaction with an interface is governed by a purely hyperbolic equation. Thus, CV model (Eq. (1)) can be transformed into

$$\tau\frac{\partial q}{\partial t} = -k\nabla T. \tag{2}$$

Consider the case where one side of the region is exposed to a pulsed heat flux which generates a thermal wave propagating forward. The solution that describes the heat flux waves can be expressed as

$$q = A\exp(i\omega t - i\vec{k}\cdot\vec{r}) \tag{3}$$

where A is the amplitude of the heat flux, ω is the frequency of the heat source and $\vec{k}$ is the wave vector.

The expressions for the three waves shown in Fig. 1 are:

for the incident wave,

$$q_i = A_i\exp(i\omega t - i\vec{k}_1\cdot\vec{r}), \tag{4.1}$$

for the reflection wave,

$$q_r = A_r\exp(i\omega t + i\vec{k}_1\cdot\vec{r}), \tag{4.2}$$

for the refraction wave,

$$q_t = A_t\exp(i\omega t - i\vec{k}_2\cdot\vec{r}), \tag{4.3}$$

where the subscripts i, r, and t respectively, represent incidence, reflection and refraction and subscripts 1 and 2 respectively, represent the thermal properties of materials I and II.

The thermal wave speed based on CV model is determined by the ratio of the thermal diffusivity to the relaxation time as

$$v = \sqrt{\alpha/\tau}. \tag{5}$$

As with the radiant energy density, the ballistic thermal energy density can be defined as the ratio of the heat flux to the thermal wave speed as

$$I_{heat} = \frac{q}{v}. \tag{6}$$

In the experiments detecting the second sound (thermal wave), the temperature profiles are always derived from the ratio of the heat flux to the thermal wave speed, as Shimazak [2] adopted the Eq. (7),

$$\Delta T_{theory} = \frac{q}{\rho c_p C_{20}}, \tag{7}$$

in his study where C_{20} is the heat perturbation speed. Analogous to Eq. (7), one kind of temperature profile fluctuations in thermal waves can be defined as

$$\Delta T_{ballistic} = \frac{q}{\rho C_V v}, \tag{8}$$

where v is the thermal wave speed based on CV model. The thermal wave conveys the ballistic thermal energy from one side to the other. In the process, the temperature fluctuations can be divided into one caused by diffusion and another caused by ballistic transport [67]

$$T = T_{ini} + \Delta T_{diff} + \Delta T_{ballistic}, \tag{9}$$

where T_{ini} represents the initial temperature of the media, ΔT_{diff} represents the fluctuations caused by diffusion and $\Delta T_{ballistic}$ represents the fluctuations caused by ballistic transport. Considering the relationship between the ballistic temperature fluctuations, $\Delta T_{ballistic}$, and the ballistic thermal energy density, I_{heat}, the ballistic thermal energy $E_{ballistic}$ is defined as

$$E_{ballistic} = \int_L \rho C_V \Delta T_{ballistic} dx = \int_L I_{heat} dx. \tag{10}$$

Combined with Eq. (6), it gives

$$E_{ballistic} = \int_L \frac{q}{v} dx. \tag{11}$$

$E_{ballistic}$ is used to describe the thermal energy propagation in the media, which is then used to study the energy distribution characteristics of the interface.

On the assumption of no interface resistance, the interface conditions satisfy

$$\begin{cases} T|_{x\to x-} = T|_{x\to x+} \\ q|_{x\to x-} = q|_{x\to x+} \end{cases}. \tag{12}$$

Ignoring the diffusion term as in Eq. (2) means that ΔT_{diff} is zero. Combining Eqs. (4.1)–(4.3) with the interface conditions (Eq. (12)) gives

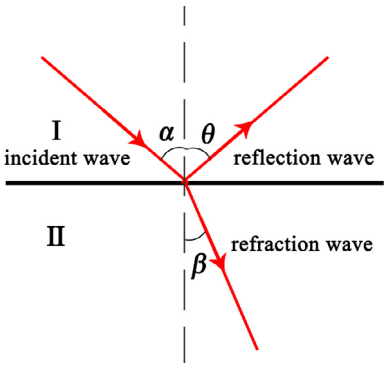

Fig. 1. Illustration of incident angle, α, reflection angle, θ, and refraction angle, β, and the relationship between the incident, reflection and refraction waves.

$$\frac{q_i}{(\rho C_v)_1 v_1} + \frac{q_r}{(\rho C_v)_1 v_1} = \frac{q_t}{(\rho C_v)_2 v_2}, \tag{13.1}$$

$$q_i \cos\alpha - q_r \cos\theta = q_t \cos\beta, \tag{13.2}$$

$$q_i \sin\alpha + q_r \sin\theta = q_t \sin\beta, \tag{13.3}$$

where α is the incident angle, θ is the reflection angle, and β is the refraction angle as shown in Fig. 1. In addition, v represents the thermal wave speed in the media and ρC_v represents the volumetric specific heat. The results can be simplified as

$$\alpha = \theta, \tag{14.1}$$

$$\frac{\sin\beta}{\sin\alpha} = \frac{v_2}{v_1}, \tag{14.2}$$

$$\frac{q_t}{q_i} = \frac{2(\rho C_v)_2 v_2 \cos\theta}{(\rho C_v)_2 v_2 \cos\beta + (\rho C_v)_1 v_1 \cos\theta}, \tag{14.3}$$

$$\frac{\Delta T_{t,ballistic}}{\Delta T_{i,ballistic}} = \frac{2(\rho C_v)_1 v_1 \cos\theta}{(\rho C_v)_2 v_2 \cos\beta + (\rho C_v)_1 v_1 \cos\theta} \tag{14.4}$$

These equations can show that the reflection angle θ is equal to the incident angle α (Eq. (14.1)), and that ratio of the sine of the refraction angle to the sine of the incident angle is identical to the ratio of the thermal wave speeds in the two materials (Eq. (14.2)). Eq. (14.3) implies the factors that influence the ratio of the heat flux amplitude of refraction wave to that of the incident wave. Eq. (14.4) shows the relationships that thermal wave speed, volumetric heat capacity and incident angle determine the amplitude of temperature fluctuations due to ballistic transport of refraction wave to that of incident wave.

The ratio of the ballistic thermal energy of the refraction wave to that of the incident wave can be derived from Eqs. (14.3) and (14.4) as

$$r = \frac{E_t}{E_i} = \int_{L_2} \frac{q_t}{v_2} dx \Big/ \int_{L_1} \frac{q_i}{v_1} dx = \frac{2(\rho C_v)_2 v_2 \cos\theta}{(\rho C_v)_2 v_2 \cos\beta + (\rho C_v)_1 v_1 \cos\theta}, \tag{15}$$

where r is called the thermal energy transmittance ratio (TETR), which represents the portion of the energy that is transmitted through the interface per unit cross sectional area. Considering the change in the cross sectional area caused by different incident angles and refraction angles, the ballistic thermal energy conveyed across the interface can be expressed as

$$\frac{E_{t,total}}{E_{i,total}} = \frac{E_t \cos\beta}{E_i \cos\theta} = \frac{2(\rho C_v)_2 v_2 \cos\beta}{(\rho C_v)_2 v_2 \cos\beta + (\rho C_v)_1 v_1 \cos\theta}. \tag{16}$$

Another important parameter is the material speed ratio (MSR), which describes how the thermal wave speeds up or slows down when propagating across the interface. It is derived from the ratio of the thermal wave speed in material II to that in material I

$$m = v_2/v_1 = \sqrt{(\alpha_2\tau_1)/(\alpha_1\tau_2)}. \tag{17}$$

For the sake of convenience, the material where the thermal waves have higher speed is called the thermally thinner medium, by analogy to an optically thinner medium, while the material where the thermal waves have relatively lower speed is called the thermally denser medium. When $m < 1$, the ballistic thermal energy propagates from the thermally thinner medium into the thermally denser medium. On the other hand, when $m > 1$, the ballistic thermal energy propagates from the thermally denser medium into the thermally thinner medium. When $m = 1$, there is no interface. The discussions in the following sections imply that MSR is one of the most significant properties of the interface. For example, the ratio of the sine of the refraction angles to that of the incident angles is identical to MSR.

Thus, regardless of boundary resistance, when thermal waves propagate across an interface,

(i) The incident wave causes two waves, namely a reflection wave and a refraction wave.
(ii) The reflection angle always equals the incident angle while the ratio of the sine of the refraction angle to the sine of incident angle equals the material speed ratio.
(iii) The thermal energy transmittance ratio can be explicitly expressed in terms of material speed ratio, heat capacity and incident angle.

3. Numerical methods and its validation

3.1. CV model

The derivative part of heat flux with respect to time in thermal wave models is responsible to the wavelike properties [68]. Zhang et al. [69] studied the damping effect of CV model, DPL model and TM model and found that a damping factor ξ, which is related to the relaxation term, could be defined to determine the damping of thermal waves. CV model, which possesses the typical characteristics of thermal waves, is adopted to simulate a two-dimensional heat conduction problem without inner heat sources. The materials are assumed to be isotropic. Eq. (1) is combined with the energy conservation equation to give

$$q_x + \tau \frac{\partial q_x}{\partial t} = -k \frac{\partial T}{\partial x}, \tag{18.1}$$

$$q_y + \tau \frac{\partial q_y}{\partial t} = -k \frac{\partial T}{\partial y}, \tag{18.2}$$

$$\rho C_v \frac{\partial T}{\partial t} + \frac{\partial q_x}{\partial x} + \frac{\partial q_y}{\partial y} = 0, \tag{18.3}$$

where q_x is the heat flux along the x direction at the node, q_y is the heat flux along the y direction at the node and T represents the node temperature. The calculation is simplified by introducing the following dimensionless parameters:

$$\begin{aligned} &x^* = x/d, t^* = t/t_0, T^* = T/T_0, q_x^* = q_x/q_0, q_y^* = q_y/q_0, \\ &k^* = k/k_0, (\rho C_v)^* = (\rho C_v)/(\rho C_v)_0, Z_q = \tau/t_0. \end{aligned} \tag{19}$$

In Eq. (19), (ρC_v) is dealt with as one parameter because ρ and C_v are always linked and play similar roles. These dimensionless values then fit:

$$\begin{cases} \frac{k_0 T_0}{d q_0} = 1 \\ \frac{q_0 t_0}{(\rho C_v)_0 T_0 d} = 1 \end{cases} \tag{20}$$

For convenience, the asterisks are uniformly omitted and the parameters discussed below are all dimensionless. Eqs. (18.1)–(18.3) can then be transformed into

$$q_x + Z_q \frac{\partial q_x}{\partial t} = -k \frac{\partial T}{\partial x}, \tag{21.1}$$

$$q_y + Z_q \frac{\partial q_y}{\partial t} = -k \frac{\partial T}{\partial y}, \tag{21.2}$$

$$\rho C_v \frac{\partial T}{\partial t} + \frac{\partial q_x}{\partial x} + \frac{\partial q_y}{\partial y} = 0. \tag{21.3}$$

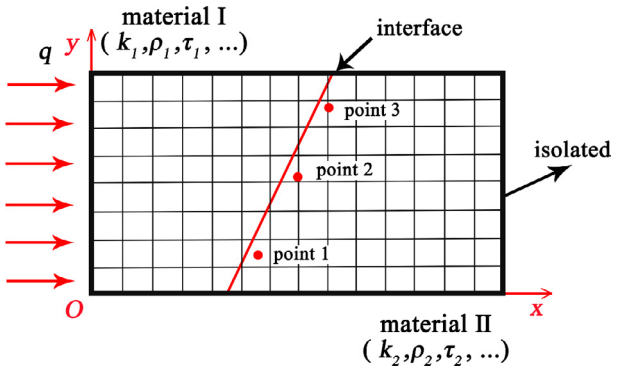

Fig. 2. Computational domain in a rectangular coordinate system with the origin at the bottom left. An inclined interface in the center divides the domain into material I and material II with different thermal properties. The energy propagation across the interface is monitored at three points after the interface. The heat pulse is imposed at the entire left boundary of material I at the beginning.

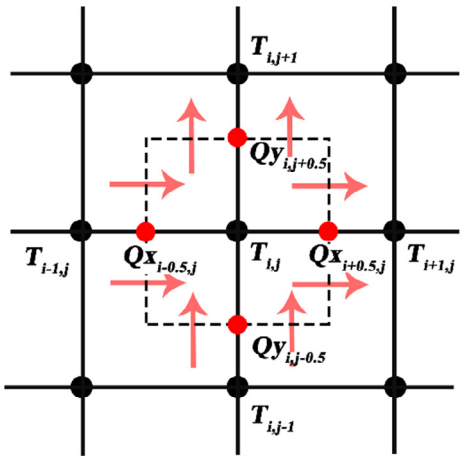

Fig. 3. Locations of the heat flux nodes and temperature nodes where the heat flux nodes are at the boundaries of the temperature control volumes.

3.2. Simulation details

The model is applied to a two-dimensional heat conduction problem in a rectangular plane with constant thermal properties. Square elements are used to divide the computational domain into 5×10^5 control volumes. The coordinate system is given in Fig. 2 and the entire system is assumed to be isotropic without inner heat sources. An oblique ideal interface is constructed between the two dissimilar materials, Material I and Material II. The incident angle is altered by changing the slope of the interface while maintaining the direction of the incident thermal wave. The thermal properties of Material I on the left side are k_1, τ_1 and ρ_1 while the properties of Material II are k_2, τ_2 and ρ_2 where k represents the thermal conductivity and τ represents the relaxation time.

The domain is initially at a steady state at temperature T_0 without any heat fluxes. All the boundaries are insulated except the left boundary where a heat pulse is applied. The heat flux and the temperature of each element are defined at different locations due to their specific distribution characteristics. Every heat flux node is positioned between two temperature nodes as shown in Fig. 3 to prevent numerical oscillations.

A heat pulse in the positive x direction is added along the entire left boundary from the beginning time. The heat flux is assumed to only influence the nodes at the boundary with little impact on the interior nodes. The four kinds of heat pulses considered here and shown in Fig. 4 are described by:

sinusoidal heat pulse

$$q|_{x=0} = \begin{cases} A \times (1 - \cos(2\pi t/t_0)) & t \leqslant t_0 \\ 0 & t > t_0 \end{cases}, \tag{22.1}$$

rectangular heat pulse

$$q|_{x=0} = \begin{cases} A & t \leqslant t_0 \\ 0 & t > t_0 \end{cases}, \tag{22.2}$$

triangular heat pulse

$$q|_{x=0} = \begin{cases} A \times \left(1 - \left|\frac{2t}{t_0} - 1\right|\right) & t \leqslant t_0 \\ 0 & t > t_0 \end{cases}, \tag{22.3}$$

ramped heat pulse

$$q|_{x=0} = \begin{cases} A\left(1 - \frac{t}{t_0}\right) & t \leqslant t_0 \\ 0 & t > t_0 \end{cases}. \tag{22.4}$$

where A is the heat pulse amplitude which was set to 1 in the simulations and the nondimensional pulse time, t_0 was set to 0.1. The

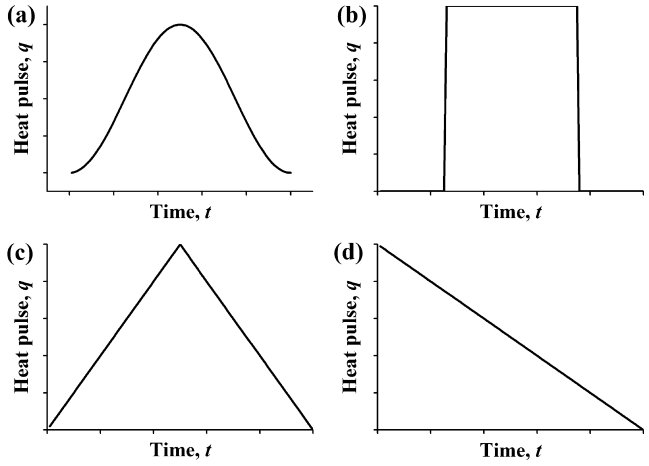

Fig. 4. Shapes of the heat pulses imposed at the left boundary: (a) sine function heat pulse, (b) rectangular heat pulse, (c) triangular heat pulse, and (d) ramp heat pulse.

nondimensional initial temperature, T_0 was set to 1 and the rectangular region was 2×1 (length $\times$ width). Other parameters used in the simulations are listed in Table 1. The thermal wave propagates from Material I into Material II across the interface where the interface conditions in Eq. (12) are satisfied.

The heat fluxes were recorded at three points in the simulations with the points located right after the interface in Material II as y equals 0.2, 0.5 and 0.8. The heat fluxes at these points cannot be directly compared because of the damping effect. The heat fluxes at these points with no interface were taken as reference values. And the ratios of the heat flux with an interface to these reference values demonstrate some key principles of this problem.

A staggered interface was used to replace the actual oblique interface. It was constructed from the nodes in the left plane (Material I) nearest to the actual interface as shown in Fig. 5. This transformation has been widely used in regular grids, because it can reduce the complexity of meshing grids.

3.3. Alternative direction implicit difference scheme

The alternative direction implicit difference scheme (ADI) was used to solve the equations [70]. ADI is often used to solve two-dimensional or multi-dimensional problems in fluid dynamics.

Table 1
Computational parameters.

Parameter	Value	Parameter	Value
Thermal conductivity, k_0 (W/K)	150	Model width, d (nm)	57.7
Specific heat, C_V (J/(K·kg)	700	Model length, l (nm)	115.4
Relaxation time, τ_0 (ps)	33.3	Initial temperature, T_0 (K)	300
Thermal diffusivity, α_0 (m^2/s)	1×10^{-4}	Heat flux amplitude, A_0 (W/s)	2.6×10^{11}
Heat pulse duration, t_0 (ps)	3.33	Density, ρ_0 (kg/m^3)	2328.3
Space interval, Δx (1)	2×10^{-3}	Time interval, Δt (1)	1×10^{-4}

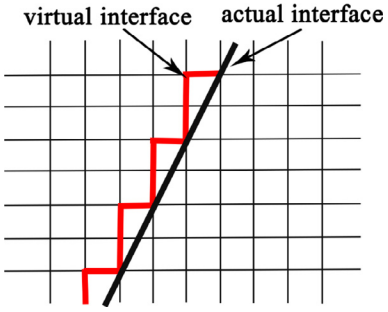

Fig. 5. Staggered interface structure and the actual interface: the nodes just left of the actual interface are connected to form the computational domain in red. (For interpretation of the references to color in this figure legend, the reader is referred to the web version of this article.)

For two-dimensional problems, it is unconditionally stable, while for multi-dimensional problems, it is conditionally stable. The algebraic equations were solved using the chasing method instead of iteration to reduce the computation time and storage space requirements.

In the method, one time step is divided into two parts from t^n to $t^{n+\frac{1}{2}}$ and from $t^{n+\frac{1}{2}}$ to t^{n+1}. T and q_x are calculated implicitly in the x direction in the first part, while T and q_y are calculated explicitly in the y direction as

$$q^{n}_{x,i+\frac{1}{2}j} + Z_q \frac{q^{n+\frac{1}{2}}_{x,i+\frac{1}{2}j} - q^{n}_{x,i+\frac{1}{2}j}}{\frac{1}{2}\Delta t} = -k \frac{T^{n+\frac{1}{2}}_{i+1,j} - T^{n+\frac{1}{2}}_{i,j}}{\Delta x}, \tag{23.1}$$

$$q^{n}_{y,ij+\frac{1}{2}} + Z_q \frac{q^{n+\frac{1}{2}}_{y,ij+\frac{1}{2}} - q^{n}_{y,ij+\frac{1}{2}}}{\frac{1}{2}\Delta t} = -k \frac{T^{n+\frac{1}{2}}_{ij+1} - T^{n+\frac{1}{2}}_{i,j+1}}{\Delta y}, \tag{23.2}$$

$$\rho C_v \frac{T^{n+\frac{1}{2}}_{i,j} - T^{n}_{i,j}}{\frac{1}{2}\Delta t} + \frac{q^{n+\frac{1}{2}}_{x,i+\frac{1}{2}j} - q^{n+\frac{1}{2}}_{x,i-\frac{1}{2}j}}{\Delta x} + \frac{q^{n}_{y,ij+\frac{1}{2}} - q^{n}_{y,ij-\frac{1}{2}}}{\Delta y} = 0. \tag{23.3}$$

Because of the staggered mesh, the locations of q_x and T are interlaced. The coefficient matrices derived from Eqs. (23.1) and (23.3) are strongly diagonally dominant.

The chasing method is a way to solve tridiagonal algebraic equation sets. The process can be expressed as

$$Bz = f, \tag{24}$$

$$z = \left[q^{n+\frac{1}{2}}_{x,\frac{1}{2}j}, T^{n+\frac{1}{2}}_{1j}, q^{n+\frac{1}{2}}_{x,\frac{3}{2}j}, \ldots, T^{n+\frac{1}{2}}_{nj}, q^{n+\frac{1}{2}}_{x,n+\frac{1}{2}j}\right], \tag{25}$$

where B is the coefficient matrix, z is a vector consisting of T and q as shown in Eq. (25) and f is the nonhomogeneous term. Then, A can be split into two matrixes as

$$B = LU, \tag{26}$$

where L is a lower triangular matrix and U is an upper triangular matrix. Both are tridiagonal matrices, which means they are bivariate diagonal. Eq. (24) can then be transformed into

$$\begin{aligned} Lw &= f, \\ Uz &= w. \end{aligned} \tag{27}$$

Then the values could be calculated one by one [71].

After the calculation of q_x and T at the $t^{n+\frac{1}{2}}$ time step, q_y is calculated using Eq. (23.2). The next half step from the time step $t^{n+\frac{1}{2}}$ to t^{n+1} is similar with T and q_y calculated implicitly in the y direction while T and q_x are calculated explicitly in the x direction as

$$q^{n+\frac{1}{2}}_{x,i+\frac{1}{2}j} + Z_q \frac{q^{n+1}_{x,i+\frac{1}{2}j} - q^{n+\frac{1}{2}}_{x,i+\frac{1}{2}j}}{\frac{1}{2}\Delta t} = -k \frac{T^{n+\frac{1}{2}}_{x,i+1\,j} - T^{n+\frac{1}{2}}_{x,ij}}{\Delta x}, \tag{28.1}$$

$$q^{n+\frac{1}{2}}_{y,ij+\frac{1}{2}} + Z_q \frac{q^{n+1}_{y,ij+\frac{1}{2}} - q^{n+\frac{1}{2}}_{x,ij+\frac{1}{2}}}{\frac{1}{2}\Delta t} = -k \frac{T^{n+1}_{x,ij+1} - T^{n+1}_{x,ij+1}}{\Delta x}, \tag{28.2}$$

$$\rho C_V \frac{T^{n+1}_{ij} - T^{n+\frac{1}{2}}_{ij}}{\frac{1}{2}\Delta t} + \frac{q^{n+\frac{1}{2}}_{x,i+\frac{1}{2}j} - q^{n+\frac{1}{2}}_{x,i-\frac{1}{2}j}}{\Delta x} + \frac{q^{n+1}_{y,ij+\frac{1}{2}} - q^{n+1}_{y,ij-\frac{1}{2}}}{\Delta y} = 0. \tag{28.3}$$

Then, the chasing method is used to solve the algebraic equation sets for q_y and T. Then q_x is calculated using Eq. (28.1). The procedure for each computation time step is summarized as:

(i) Discretize the partial differential equation set into nodal algebraic equation sets, explicitly in the y direction and implicitly in the x direction for the heat flux and the temperature in time step $t^{n+\frac{1}{2}}$.
(ii) Solve the tridiagonal system for q_x and T using the chasing method in time step $t^{n+\frac{1}{2}}$.
(iii) Calculate q_y from q_x and T in time step $t^{n+\frac{1}{2}}$.
(iv) Discretize the partial differential equation sets into nodal algebraic equation sets in the other direction, explicitly in the x direction and implicitly in the y direction for the heat flux and the temperature in time step t^{n+1}.
(v) Solve the tridiagonal system for q_y and T using the chasing method in time step t^{n+1}.
(vi) Calculate q_x from q_y and T in time step t^{n+1}.

The calculations then advance one time step forward. This scheme adopted has second order accuracy in space and first order accuracy in time. The conditions for convergence are that the matrix is strongly diagonally dominant,

$$\min(Z_q/k, \rho C_V) \geqslant \max\left(\frac{\Delta t}{\Delta x}, \frac{\Delta t}{\Delta y}\right). \tag{29}$$

This method is robust and efficient with fewer iterations, so that more nodes can be included to increase the simulation accuracy.

3.4. Validation

A one-dimensional example was used to verify the validity of the computational method. The heat flux and temperature varia-

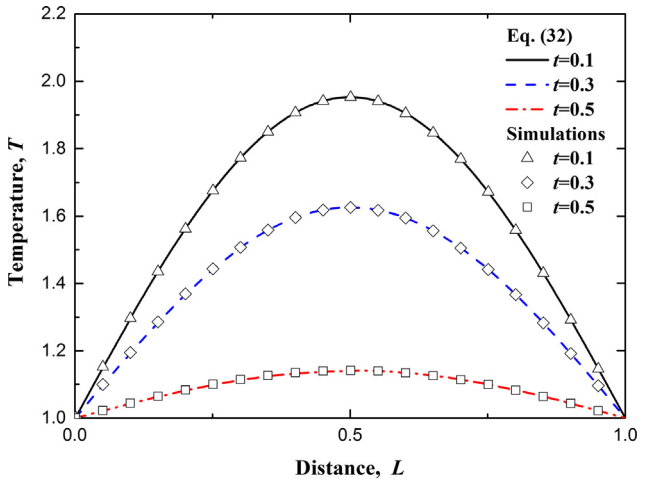

Fig. 6. Comparisons of the analytical solution (curves) with simulation results for a one-dimensional heat conduction problem (symbols).

tions were assumed to be modeled by CV model with initial temperature gradients. The initial temperature distribution was

$$T(x,0) = T_0 + T_0 \sin\left(\frac{\pi x}{L}\right), \frac{\partial T(x,0)}{\partial t} = 0. \quad (30)$$

The boundary conditions were isothermal,

$$T(0,t) = T_0, T(L,t) = T_0. \quad (31)$$

The exact solution can be derived by the method of separation of variables [72],

$$T(x,t) = T_0 \exp\left(-\frac{t}{2\tau}\right) \sin\left(\frac{\pi x}{L}\right)\left[\cos(\lambda t) + \frac{1}{2\tau\lambda}\sin(\lambda t)\right], \quad (32)$$

where $\lambda = \sqrt{\frac{n^2\pi^2 a}{\tau L^2} - \frac{1}{4\tau^2}}$.

As shown in Fig. 6, the simulation results of the ADI algorithm in this one-dimensional problem agree well with the analytical solution, implying that the method is valid. The grid independence was verified using the results with the present space interval, 2×10^{-3}, and time interval, 1×10^{-4} as reference. The relative error was calculated as the percentage of the deviation of the peak of the heat flux and the temperature at time t=0.5 from the standard. The relative errors listed in Table 2 show that the space step and time step are reasonable. The excellent agreement with the theoretical solution and the grid independence mean that the scheme is reliable.

4. Simulation results and discussion

4.1. Normal incidence

Normal incidence was investigated with the material interface parallel with the wavefront of the thermal wave. Considering the relationships between the heat flux and the ballistic temperature fluctuations in Eqs. (8)–(11), the temperature profiles and the heat flux profiles are both used to describe the reflection and refraction phenomena. An interface was constructed by changing the thermal conductivity, k of both materials while keeping the other properties constant. The MSR was derived from the square root of the ratio in Eq. (5).

Fig. 7 shows jumps in the peak values of both the temperature and heat flux profiles at the interface. The peak is known to dissipate during the process. For $m < 1$, which means that the thermal wave propagates from a thermally thinner medium into a thermally denser medium, the peak temperature of the refraction wave is higher than that of the incident wave. At the same time, a positive reflection wave begins to propagate in the negative x direction. The positive reflection temperature wavefront means that part of the ballistic thermal energy conveyed by the thermal wave is reflected and the area in the left of the interface will be heated once again by the reflection wave. This phenomenon is called a hot reflection wave. Actually, material II has less ability to convey the thermal energy than material I, so only part of the ballistic thermal energy is transported through the interface and the rest is reflected back. For this reason, the slower propagation of energy results in a higher temperature peak. The heat flux curves in Fig. 7(b) show a drop after the interface, which means that the peak heat flux in the refraction wave is lower than that in the incident wave. In addition, there is a negative reflection wave for the heat flux. The negative values mean that the reflection wave is propagating in the negative x direction because the heat flux is actually a vector. When $m > 1$, which means that the thermal wave propagates from a thermally denser medium into a thermally thinner medium, the results become much more interesting. The temperature peaks of refraction wave are lower and the amplitude of the reflected wave is negative, which means the temperature is lower than ambient temperature. It implies that the area in the left of the interface will be cooled by the reflection thermal wave, so this phenomenon is called a cool reflection wave. The heat flux profiles of refraction wave have a higher peak and there is a reflection heat flux wave with positive amplitude. The positive values indicate that the heat flux direction is opposite to the thermal wave propagation direction. The reflection wave results in a tendency of ballistic thermal energy conveyed along the positive direction of the x axis. The energy transmitted through the interface for this case is then more than that of the incident wave. The reasons are that the governing Eq. (1) and the interface conditions Eq. (12) must be satisfied at the same time. The thermal wave in material II has a higher speed, thus, it is able to convey energy more rapidly. However, the heat flux remains the same on both sides, which means that the ballistic thermal energy density decreases after the interface in Eq. (6), which reduces the peak of the temperature fluctuations and leads more energy to propagate through the interface. Because more energy passes through the interface, the area before the interface have to generate a heat flux to make up for the lost energy to maintain the thermal equilibrium. This then creates a cool reflection wave. The sudden increase of the heat flux peak in Fig. 7(d) at about $x = 1$ is caused by the overshooting from the boundary reflection [37].

Thermal energy transmittance ratio r, is introduced to get a quantitative estimation of the ballistic thermal energy transfer across the interface. When a solitary wave moves forward in the medium, the integral of the wave profile over time at one point G_{time} and the integral of the wave profile in space at one time G_{space} are related as

Table 2
Grid independence validation.

Spatial steps (Δx)	1×10^{-2}	5×10^{-3}	2.5×10^{-3}	1×10^{-3}	2×10^{-4}
Error in q (%)	3.72	0.14	4.90×10^{-2}	7.89×10^{-2}	9.39×10^{-2}
Error in T (%)	2.66	0.22	1.41×10^{-2}	3.98×10^{-3}	8.00×10^{-3}

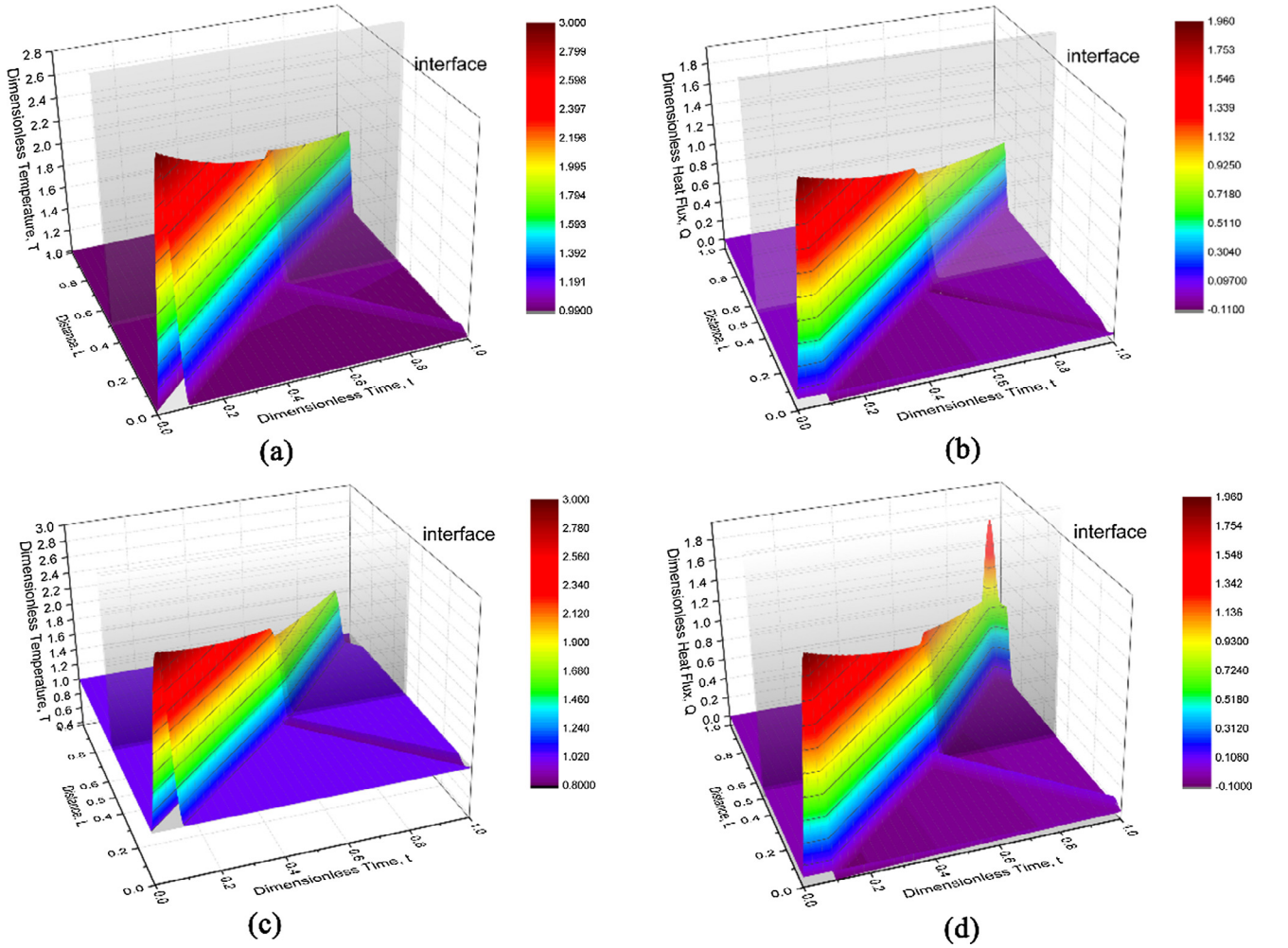

Fig. 7. Locations from the y axis and the peak values of the maximum temperatures and heat fluxes along the thermal wavefront at various times and material speed ratios. (a) Temperatures at $m = 0.8$, (b) heat fluxes at $m = 0.8$, (c) temperatures at $m = 1.5$ and (d) heat fluxes at $m = 1.5$.

$$G_{\text{time}} = \int_T \frac{A\exp(i\omega t - ikx)}{c} dt = \frac{\omega}{k} \int_L \frac{A\exp(i\omega t - ikx)}{c} dx = \frac{\omega}{k} G_{\text{space}}. \tag{33}$$

The ballistic thermal energy is mainly conveyed by the thermal waves, as shown in Eqs. (8)–(11). Thus, the spatial integral can be transformed into a temporal integral to eliminate the difficulty of accumulating ballistic thermal energy in space. Another advantage of this method is that it can help avoid the influence of dissipation during the propagation and focus only on the impact of the interface. To get the ballistic thermal energy of the incident wave at the interface, a blank control group is defined where there is no interface and the ballistic thermal energy is detected at the same positions.

From Eq. (15), when the incident angle is zero, the TETR r obeys

$$r = \frac{E_t}{E_i} = \frac{2(\rho C_v)_2 v_2}{(\rho C_v)_2 v_2 + (\rho C_v)_1 v_1} \tag{34}$$

The MSRs are changed by changing either the thermal conductivity ratios of the materials or the relaxation time ratios while the other parameters remain unchanged. Fig. 8 shows how the MSRs influence the thermal energy transmittance ratio r. The discrete points representing the numerical results agree well with the curve predicted by the theoretical model. The ratio, r increases with increasing material speed ratio, and when m equals 1, r also equals 1. When $m > 1$, the thermal energy transmittance ratio is larger than 1, which means that more energy is transmitted than the total incident ballistic thermal energy. It demonstrates that the most important property is the MSR, not the thermal conductivity ratio or the relaxation time ratio alone.

4.2. Oblique incidence

4.2.1. Shapes and direction

The wave directions are altered after reflection and refraction at the interface. The temperature profiles of thermal waves with an incident angle of 45° are shown in Fig. 9, where the material speed ratios are 0.8 and 1.22. The inclined gray plane represents the interface. The reflection wave is labeled in the figure and the refraction part is easy to distinguish. The reflection wave is light green[1] for $m = 0.8$, showing that the temperature is higher than the ambient temperature in blue. The reflection wave is purple for $m = 1.22$, implying a lower temperature. The behaviors are similar with what happens with normal incidence, with some difference. One difference is the direction of the refraction wave and reflection

[1] For interpretation of color in Fig. 9, the reader is referred to the web version of this article.

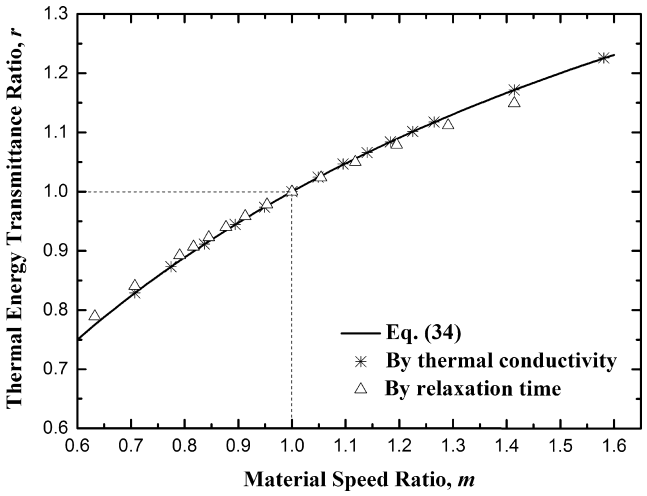

Fig. 8. Thermal energy transmittance ratios predicted by the theoretical model and the numerical simulations for various material speed ratios which were changed by altering the thermal conductivity ratio and by altering the relaxation time ratio of the materials.

wave. The wave directions are determined by the wavefront as the propagation direction is adopted perpendicular to the thermal wavefront. For $m = 1.22$, the refraction angle is larger than the incident angle, with a cold reflection wave propagating along the y axis. For $m = 0.8$, the refraction angle is smaller than the incident angle, inclining downward. There is then a hot reflection wave propagating along the y axis. When the thermal waves are reflected and refracted at the interface, the shapes of the incident wave are changed. As discussed in Section 4.1, when $m > 1$, which means that the thermal wave propagates from the thermally denser medium into the thermally thinner medium, the temperature profile peak for refraction wave is supposed to be lower than that of the incident wave at normal incidence. However, this is not true in Fig. 9(d)--(f) where the peak is obviously higher. As shown in Eq. (14.4), the difference is caused by the influence of the incident angle. More precisely, for $m = 1.22$, there is a negative amplitude wave trough following the refraction wavefront, which implies that the shape of the incident wave cannot be maintained. In that case, the temperature profiles of the refraction wave are no longer sine functions, but with something additional. That is the reason why the wave peaks are not used to study the energy propagation, but the integral of all the ballistic thermal energy is more representative.

The conditions were altered to analyze the factors influencing reflection angles. Results are given in Fig. 10(a) for various material speed ratios, m, and incident angles of 45°, 39° and 31°. Some of the reflection waves were too weak, so their directions were not easy to identify. The results fall along three horizontal lines, which shows that the reflection angles are not a function of the MSR. The positions of the lines show that the reflection angles are always the same as the incident angles. In Fig. 10(b), the incident angles vary, for different material speed ratios, forming a single inclined line with almost all the points along it. The slope of the line is 1 which indicates that the reflection wave angles are always equal to the incident wave angles for various MSRs and incident angles.

The results for the refraction angles are given in Fig. 11(a) for various MSRs and incident angles of 45°, 39° and 31°. Fig. 11(b) shows that the incident angles vary for material speed ratios of

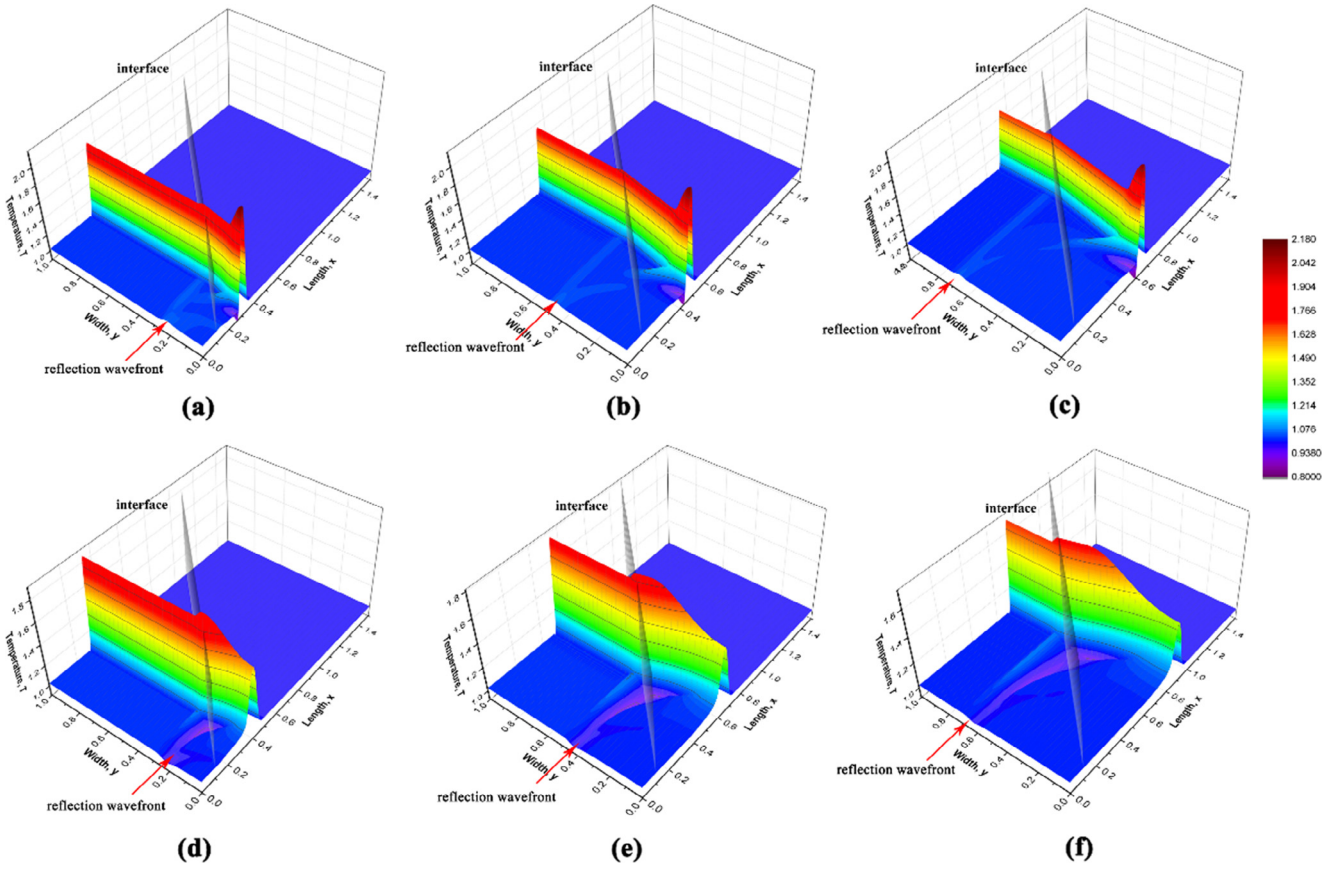

Fig. 9. Temperature profiles of the thermal wave as it propagates through the interface with an incident angle of 45°: (a–c): material speed ratio $m = 0.8$, dimensionless time $t = 0.4$, 0.6, and 0.8 and (d–f): material speed ratio $m = 1.22$ and dimensionless time $t = 0.4$, 0.6, 0.8.

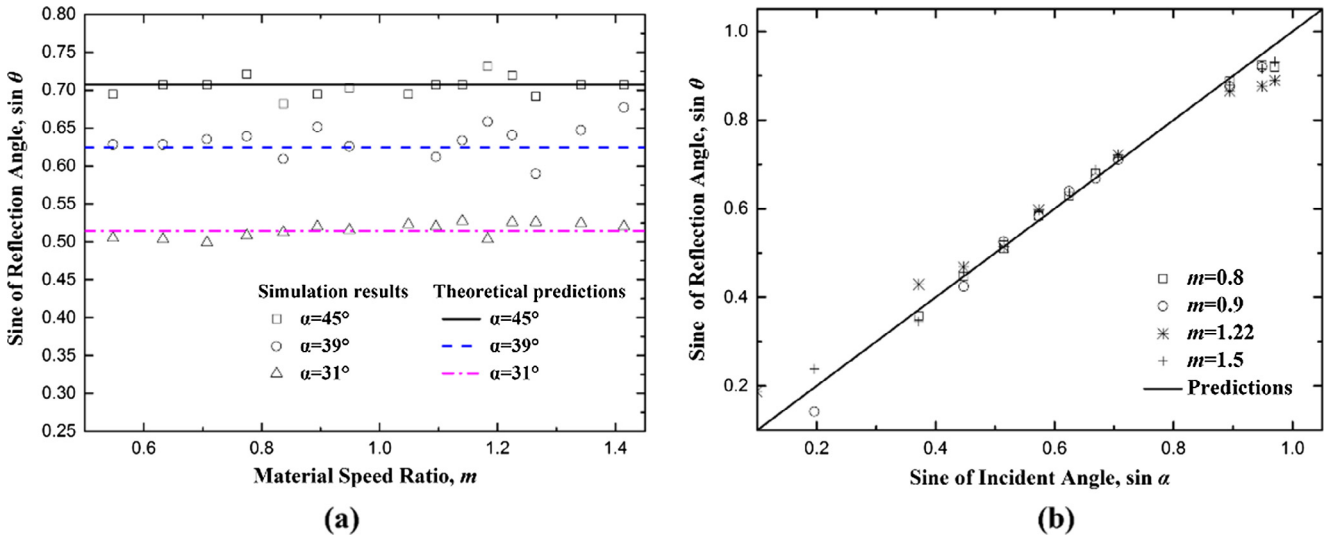

Fig. 10. Reflection wave angles under the conditions of: (a) various material speed ratios, m, with incident angles of 45°, 39°, and 31°; (b) various sines of the incident angles, sin α, with various MSRs of m = 0.8, 0.9, 1.22 and 1.5.

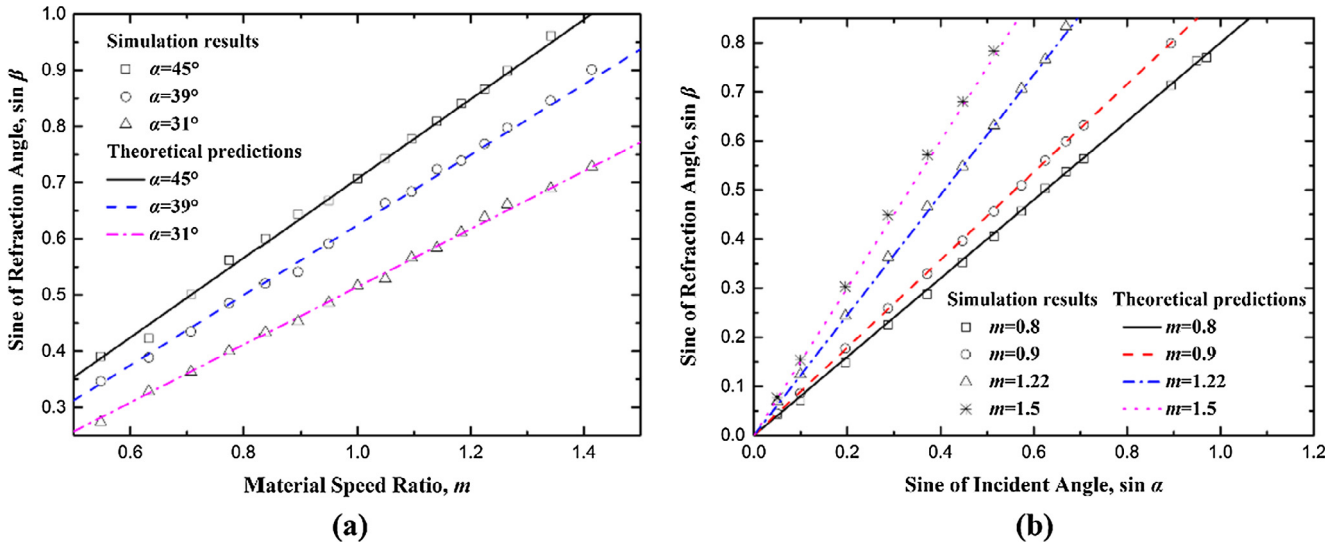

Fig. 11. Refraction wave angles under the conditions of: (a) various material speed ratios, m, with incident angles of 45°, 39°, and 31° and (b) various sines of the incident angles, sin α, with various MSRs of m = 0.8, 0.9, 1.22, and 1.5.

m = 0.8, 0.9, 1.22 and 1.5 with the data forming four separate inclined lines with different slopes. Comparison with the values predicted by the theoretical model, Eq. (14.2), shows that the sine of the refraction angles is directly proportional to the sine of the incident angles. Further investigation shows that the ratio of the sine of these two angles is equal to the material speed ratio, m. Therefore, Snell's law still governs the direction changes.

4.2.2. Energy distribution

From the theoretical model, Eq. (15) suggests the significant factors influencing the thermal energy transmittance ratio, r, are the thermal conductivity, volumetric heat capacity, relaxation time and incident angle. Among them, the thermal conductivity and the relaxation time change the interface characteristics by changing the material speed ratio. The volumetric heat capacity influences both the thermal wave speed, v, and the ballistic temperature amplitude, $\Delta T_{\text{ballistic}}$. Therefore, these effects are analyzed individually.

First, the material thermal conductivities were altered while the other parameters were kept constant. The results in Fig. 12 for incident angles of 45°, 39° and 31° show that the thermal energy transmittance ratio, r, increases as MSR increases. Three individual curves are formed for the different incident angles. They intersect at m = 1, r = 1, which means that the interface does not exist for m = 1. For m < 1, the theoretical predictions agree well with the simulation results. However, when m > 1, there are significant deviations. One of the reasons causing the differences is the change of the wave shape when m > 1, with more details shown in Fig. 13. When the thermal wave propagates from the thermally denser medium into the thermally thinner medium namely for m > 1, a negative reflection wave amplitude develops as indicated by the dark purple. The energy distribution, which is labelled by different colors, is then not homogeneous along the wavefront. Another reason for the differences when m > 1 is that the refraction wave propagates along the inclined interface upwards and interacts with other parts of the incident wave. It is difficult to distinguish them

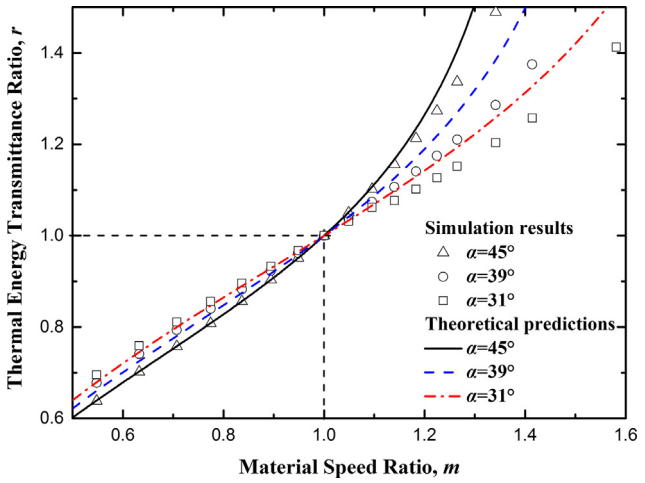

Fig. 12. Simulation results and theoretical predictions of the thermal energy transmittance ratio, r, with various material speed ratios and incident angles, α.

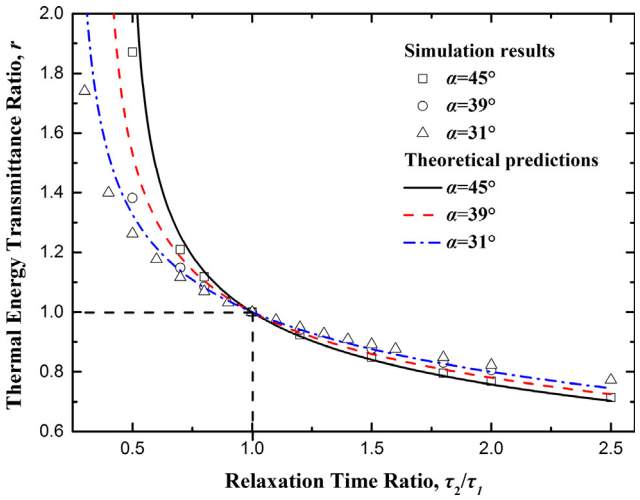

Fig. 14. Simulation results and theoretical predictions of the thermal energy transmittance ratio, r, with various relaxation time ratios and incident angles, α.

out. Thus, the effects of the factors on the thermal energy transmittance ratio for oblique incidence are much more complex than normal incidence. The TETR of waves with smaller incident angles gets larger for $m < 1$ but gets smaller for $m > 1$.

The impact of the relaxation time ratio was investigated while keeping the other parameters constant. The simulation results are compared with the theoretical predictions in Fig. 14. The tendencies are the same with the impact of thermal conductivity ratio. There are some differences for three different incident angles. The curves intersect at a relaxation time ratio of 1. The ratio, r, decreases as the relaxation time ratio increases. As shown in Eq. (5), the thermal wave speed is inversely proportional to the relaxation time. When the relaxation time ratio is lower than 1, the thermal wave accelerates after the interface and more energy is conveyed. The principles relating the thermal waves to the thermal conductivity agree well with those for the relaxation time, indicating that the MSR is a useful parameter for simplifying the problem.

The influence of the incident angle was also studied. For convenience, the incident wave angle was kept constant while the interface slope was changed to get different incident angles. Fig. 15 shows the influence of the incident angle for various material speed ratios. The simulations agree well with the theoretical predictions and it shows that the curves are strongly influenced by the material speed ratio. When the thermal wave propagates into the thermally denser medium from the thermally thinner medium ($m < 1$), the thermal energy transmittance ratio is lower than 1 and decreases with increasing incident angle. There is a sharp decrease when the incident angle reaches around 60°. For $m > 1$, r is higher than 1 and increases with increasing incident angle. As the angle approaches the critical angle for total reflection (more details are given in Section 4.3), r increases sharply. Therefore, the incident angle is also a significant factor affecting the thermal energy transmittance ratio. When $m > 1$, a relatively large incident angle is better. However, when $m < 1$, normal incidence conveys more energy.

The volumetric heat capacity, ρC_v, changes both the thermal wave speed and the ability to store thermal energy. Thus, the above discussions about the temperature and heat flux profiles are not as appropriate, as shown in Fig. 16. Both the density and the specific heat influence the volumetric heat capacity and they play similar roles. So in the simulations, only the specific heat, C_v, was varied while the density was kept constant. The specific heat capacity ratios of the two materials were set to 1.56 and 0.67, which means that the material speed ratios determined by the volumetric heat capacity are 0.8 and 1.22 corresponding to Fig. 9. The incident angle is 45°. The results show that the material

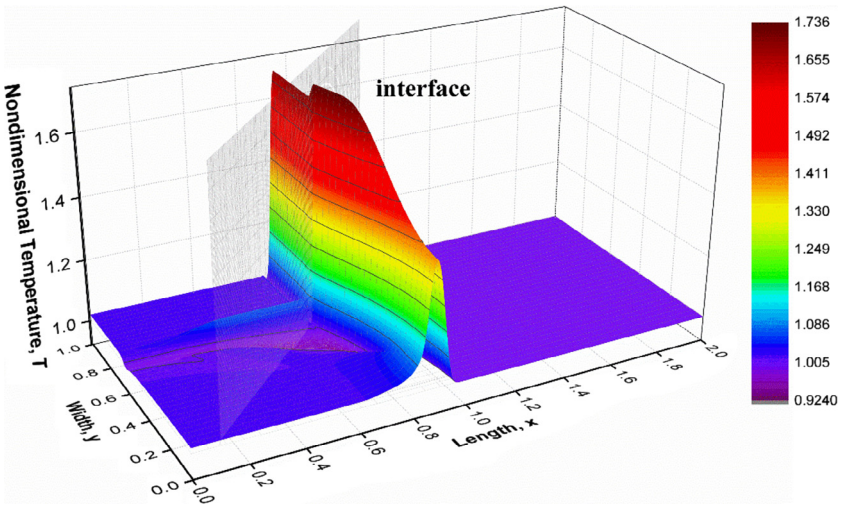

Fig. 13. Temperature profile of the thermal waves with $m = 1.22$, α=45°, $t = 0.8$. The semitransparent plane is the inclined interface.

speed ratio determines the direction of reflection wave and refraction wave as in Fig. 9. For m = 0.8, the reflection wave is a cold wave here while it was a hot one in Fig. 9. The temperature peak of the refraction wave is lower here than that of the incident wave, which also influences the energy distribution. For m = 1.22, the refraction wave and the reflection wave behave similarly to those in Fig. 9. However, the temperature peak of the refraction wave is higher here than in Fig. 9 which then conveys more reflected energy. The energy analysis shows the reasons. Fig. 17 displays the energy distributions for the three thermal waves at different incident angles of 45°, 39°, and 31°. As the ratio of the volumetric heat capacity increases, the thermal energy transmittance ratio, r, initially decreases and then increases, creating a minimum point. The TETR will reach its minimum point when the ratio of the volumetric heat capacity satisfies

$$r_{\min} = \tan^2 \alpha. \tag{35}$$

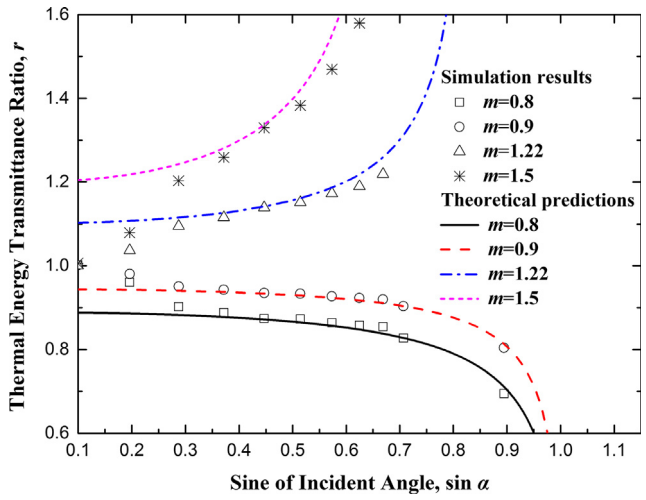

Fig. 15. Simulation results and theoretical predictions of the thermal energy transmittance ratio, r, with various incident angles and material speed ratios, m.

Three curves are formed for the three incident angles that intersect at a volumetric heat capacity ratio of 1. When the volumetric heat capacity ratio is less than 1, thermal waves with larger incident angles have higher transmittance ratios. However, when the volumetric heat capacity ratio is larger than 1, the thermal waves with larger incident angles have lower transmittance ratios. The curves have a sharp change as the specific heat ratio decreases until total reflection occurs. There are large differences between the simulations and the theory near the sharp change. However, the predictions give the right tendencies and scale.

The thermal conductivity, k, and the specific heat, C_v, were both changed while the thermal diffusivity, α, was kept constant to further understand the effects. According to Eq. (5), the thermal wave speeds will be the same in both media, so there will be no direction change. Eq. (15) can be rewritten as

$$r = \frac{E_t}{E_i} = \frac{2(\rho C_v)_2}{(\rho C_v)_2 + (\rho C_v)_1} = \frac{2k_2}{k_2 + k_1}. \tag{36}$$

Reflection waves still exist because there is difference between the energy conveyed by the refraction wave and the incident wave. A reflection wave is necessary to maintain energy conservation. The relationship between the ballistic thermal energy of the incident wave and that of the refraction wave is simply a function of the volumetric heat capacity or the thermal conductivity. These two variables both vary to keep a constant thermal diffusivity. When the ratio of the thermal conductivity of the materials increases, r increases as shown in Fig. 18. Different incident angles have little influence on the energy distribution, so the points all fall onto one curve. This suggests a basic relationship between the thermal wave speed and the energy distribution in the waves, regardless of the other parameters such as the incident angle. This phenomenon requires further understanding of the thermal waves.

4.2.3. Applicability of the principles

The boundary heat pulse was a sine function in time in former sections. However, most disturbances are not sine functions, but have all kinds of shapes. Fourier decomposition can be used to deal with complex shapes by transforming a complex heat pulse shape into a series of sine and cosine functions,

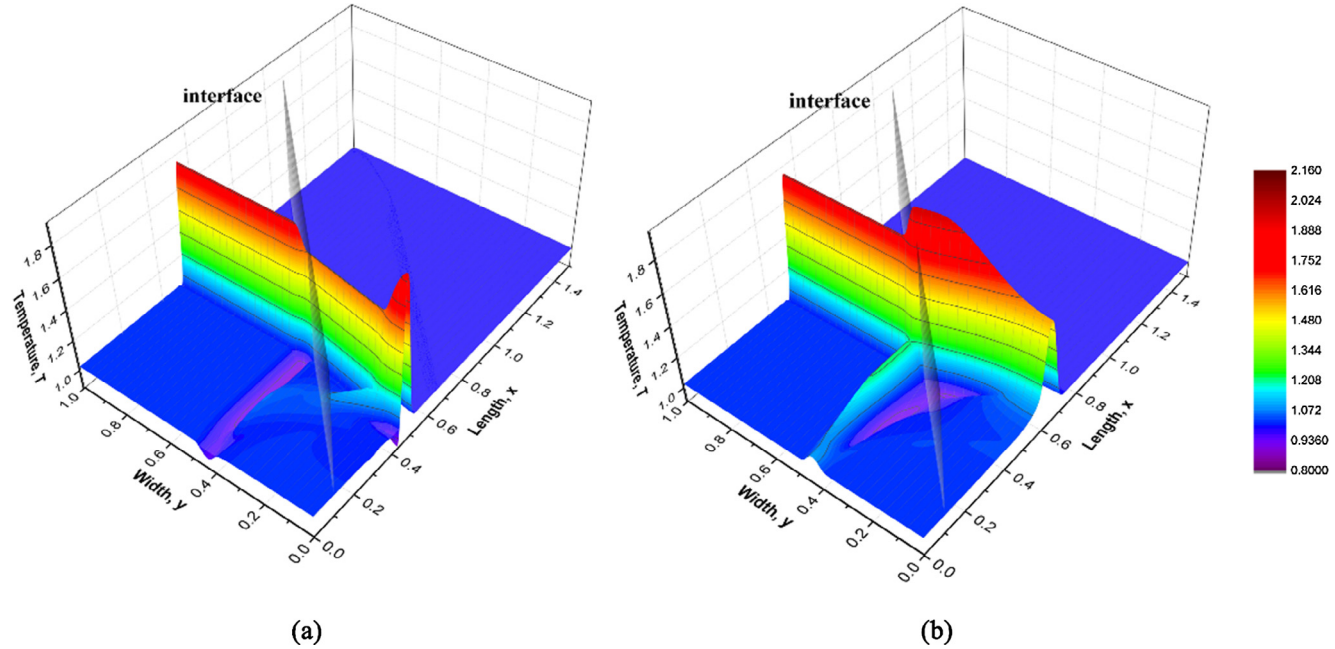

Fig. 16. Temperature profiles due to the refraction and reflection waves at time t = 0.6 for an incident angle, α, of 45° and specific heat ratios of (a) 1.56 and (b) 0.67.

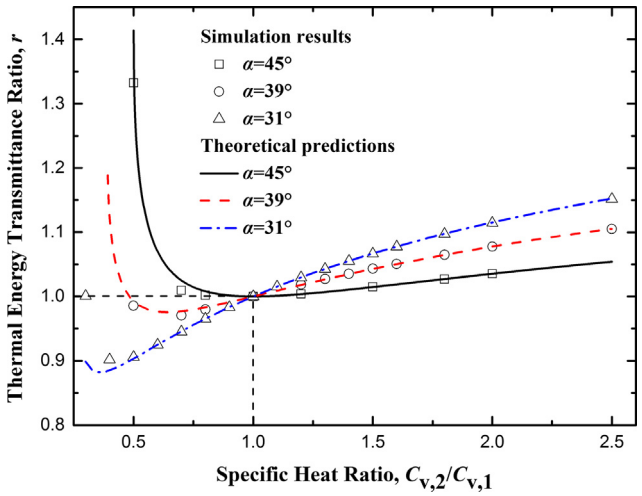

Fig. 17. Simulation results and theoretical predictions of the thermal energy transmittance ratio, r, with various specific heat ratios and incident angles, α.

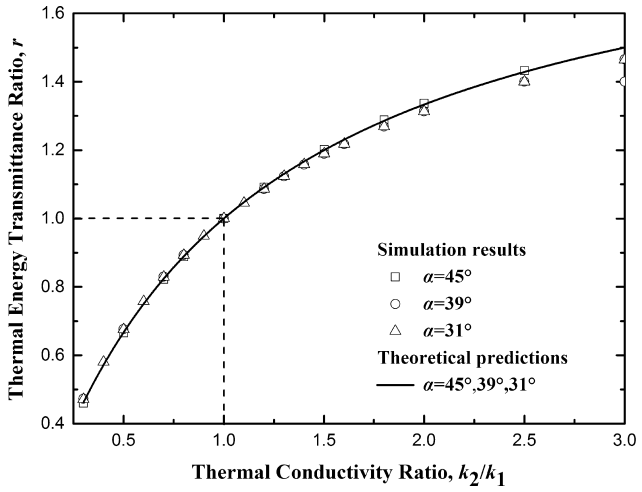

Fig. 18. Simulation results and theoretical predictions of the thermal energy transmittance ratio, r, for various thermal conductivity ratios and incident angles when the thermal diffusivity is kept constant.

$$f(t) = a_0 + \sum_n a_n \sin(n\omega t) + \sum_n b_n \cos(n\omega t), \tag{37}$$

where

$$\begin{cases} a_0 = \int_T f(t)dt \\ a_n = \int_T f(t)\sin(n\omega t)dt \\ b_n = \int_T f(t)\cos(n\omega t)dt \end{cases}, \tag{38}$$

$$T = \frac{2\pi}{\omega}. \tag{39}$$

Simulations to testify the applicability of the principles used a rectangular wave, a triangular wave and a ramp wave as incident waves. As demonstrated before, the most important feature of the interface is the MSR. Thus, in the simulations, the material speed ratio was altered while the incident angle was kept 45° and the other parameters were constant.

The predictions with the series of sine waves agree well with the simple functions in Fig. 19; thus, the principles deduced from the sine function thermal wave can be extended to arbitrary shapes. At least for this simple case, Fourier decomposition is effective and the waves show good linearity for superposition. Therefore, the thermal wave shapes do not significantly affect the energy distribution at the interface. Further confirmation is required to show this in a wide range of conditions.

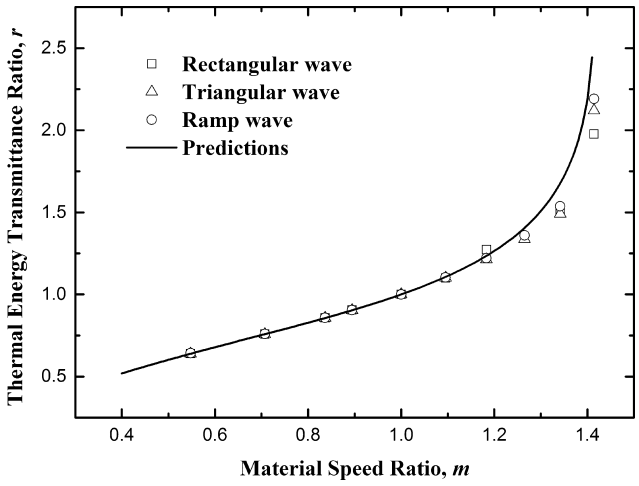

Fig. 19. Simulated thermal energy transmittance ratios for a rectangular wave, a triangular wave and a ramp wave compared with models using a series of sine function heat pulses.

4.3. Total reflection

When light propagates from an optically denser medium to an optically thinner medium and the incident angle is greater than the critical value, total reflection occurs. Similarly, when a thermal wave propagates from a thermally denser medium to a thermally thinner medium, total thermal wave reflection (simply called total reflection as well) might also occur. As Eq. (16) shows, when $\cos\beta$ reaches zero, there is no energy transmitted across the interface, although when $v_2 > v_1$, the thermal energy transmittance ratio r is larger than one. Based on Eq. (14.2) which relates the refraction angle and the incident angle, the critical angle beyond which total reflection occurs can be expressed as

$$\theta_{\text{critical}} = \arcsin\left(\frac{v_1}{v_2}\right). \tag{40}$$

When the incident angle reaches the critical value, $\cos\beta$ is equal to zero and the total refraction ballistic thermal energy is zero.

The temperature profiles better represent the ballistic thermal energy than the heat flux profiles. Actually, when total reflection occurs, the energy transmitted across the interface is not remarkably reduced. According to Section 4.1, the reflection wave is a cold reflection wave that conveys energy in the direction opposite to the propagation direction of reflection wave. Unlike for light or sound, the thermal wave energy is determined by the wave amplitude, not by the square of the amplitude. Therefore, the wave phase is significant. In optics, a half-wave loss occurs when light propagates from an optically thinner medium into an optically denser medium. However, the energy conveyed is not changed. The principles are not the same for thermal waves where the wave phase plays an important role. The refraction wave in Fig. 20 does not have a wavefront, but energy still propagates across the interface as a positive temperature fluctuation. The intersection between the incident wavefront and the interface has a temperature peak that moves along the interface. The cold reflection wave has a positive temperature fluctuation moving in front of the wave trough. Since there is no wavefront for the refraction wave, the ballistic thermal energy cannot be calculated in the usual way. This

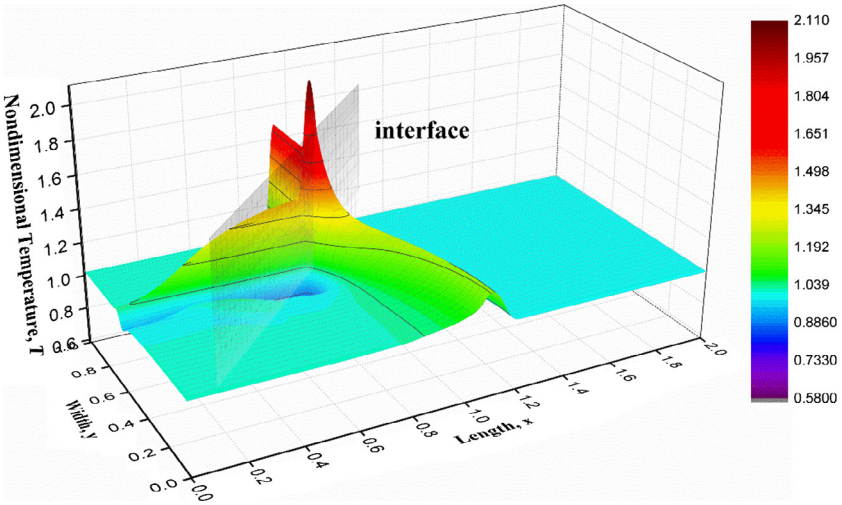

Fig. 20. Temperature profiles with total reflection with an incident angle of 45°, material speed ratio m of 2.24, and time $t = 0.8$.

phenomenon is interesting and requires further investigation to understand the nature of ballistic thermal energy transport.

5. Conclusions

The thermal behaviors of a two-layer slab with perfect contact were studied both numerically and theoretically based on CV model. The numerical simulations dealt with a two-dimensional heat conduction problem in a rectangular region with the equations solved by the alternative direction implicit method with a staggered mesh. The chasing method is used to solve the equation set instead of iterations which significantly reduces the computational times with good numerical stability. The scheme is effective, robust and relatively accurate, and can be easily extended to other thermal wave models. The interface theory neglects the diffusion term and uses the traveling wave method. Moreover, a set of theoretical equations is given to describe the principles that the phenomena of reflection and refraction at the interface of the thermal waves obey.

The temperature fluctuations are analyzed with the concept of ballistic thermal energy, which is used to describe the thermal energy flow in the media, as one of the main features of wave propagation. The thermal energy transmitted across the interface is found by transforming the space-domain integral into a time-domain integral. This method avoids the influences of damping and dispersion to show the interface characteristics clearly.

The thermal wave transport principles when crossing an interface were investigated from the aspects of shapes, directions and energy distribution. When a thermal wave propagates from a thermally thinner medium into a thermally denser medium, the temperature peak will rise while the heat flux peak will fall and the reflection wave will be a hot reflection wave. When the thermal wave propagates from a thermally denser medium into a thermally thinner medium, the temperature peak will fall while the heat flux peak will rise which indicates a cold reflection wave. The reflection angle is always the same as the incident angle, while the ratio of the sine of the refraction angle to the sine of the incident angle is always identical to the MSR, which is the ratio of thermal wave speed in material II to that in material I. An equation for the energy distribution was developed based on the wave model that indicates that the energy distribution is a function of the MSR, the volumetric heat capacity and the incident angle. Comparisons between the theoretical model and simulation results show that this equation accurately describes the energy distribution after refraction and reflection. The model also shows that the ballistic thermal energy of refraction wave can exceed that of the incident wave, which is very interesting and needs further investigation. Total reflection of the thermal wave exists, but part of the ballistic thermal energy still propagates across the interface and the reflection wave is a cold wave, which cannot convey all the energy obviously. The temperature profiles show positive temperature fluctuations before the wave trough of the reflection wave, which differs from electromagnetic waves and mechanical waves. This paper provides important guidance for thermal energy control in multilayered composite materials. Thermal wave behaviors at the interface can be used to control thermal energy distributions in structures such as thermal energy collectors and thermal diodes.

Acknowledgements

This work was financially supported by the National Natural Science Foundation of China (Grant Nos. 51676108 and 51356001), and Science Fund for Creative Research Group (No. 51621062).

Conflict of interest

We declare no any interest conflict.

References

[1] D.D. Joseph, L. Preziosi, Heat waves, Rev. Mod. Phys. 61 (1) (1989) 41–73.
[2] T. Shimazaki, M. Murakami, T. Iida, Second sound wave heat transfer, thermal boundary layer formation and boiling: highly transient heat transport phenomena in He II, Cryogenics 35 (10) (1995) 645–651.
[3] V. Peshkov, Second sound in helium II, J. Phys. 8 (1944) 381.
[4] D.S. Tang, Y.C. Hua, B.Y. Cao, Thermal wave propagation through nanofilms in ballistic-diffusive regime by Monte Carlo simulations, Int. J. Therm. Sci. 109 (2016) 81–89.
[5] H.L. Lee, W.L. Chen, W.J. Chang, Y.C. Yang, Estimation of surface heat flux and temperature distributions in a multilayer tissue based on the hyperbolic model of heat conduction, Comput. Methods Biomech. Biomed. Eng. 18 (14) (2015) 1525–1534.
[6] J. Zhou, Y. Zhang, J.K. Chen, Non-Fourier heat conduction effect on laser-induced thermal damage in biological tissues, Numer. Heat Transf. Part A: Appl. 54 (1) (2008) 1–19.
[7] M. Jaunich, S. Raje, K. Kim, K. Mitra, Z. Guo, Bio-heat transfer analysis during short pulse laser irradiation of tissues, Int. J. Heat Mass Transf. 51 (23–24) (2008) 5511–5521.
[8] W.Q. Lu, J. Liu, Y. Zeng, Simulation of the thermal wave propagation in biological tissues by the dual reciprocity boundary element method, Eng. Anal. Boundary Elem. 22 (3) (1998) 167–174.
[9] K. Ramadan, M. Al-Nimr, Thermal wave reflection and transmission in a multilayer slab with imperfect contact using the dual-phase-lag model, Heat Transf. Eng. 30 (8) (2009) 677–687.

[10] B.L. Wang, J.C. Han, A crack in a finite medium under transient non-Fourier heat conduction, Int. J. Heat Mass Transf. 55 (17–18) (2012) 4631–4637.
[11] W.J. Yao, B.Y. Cao, Thermal wave propagation in graphene studied by molecular dynamics simulations, Chin. Sci. Bull. 59 (27) (2014) 3495–3503.
[12] S. Lee, D. Broido, K. Esfarjani, G. Chen, Hydrodynamic phonon transport in suspended graphene, Nat. Commun. 6 (2015) 6290.
[13] A. Banerjee, A.A. Ogale, C. Das, K. Mitra, C. Subramanian, Temperature distribution in different materials due to short pulse laser irradiation, Heat Transf. Eng. 26 (8) (2005) 41–49.
[14] Y.K. Koh, Y. Cao, D.G. Cahill, D. Jena, Heat-transport mechanisms in superlattices, Adv. Func. Mater. 19 (4) (2009) 610–615.
[15] M. Bertolotti, G. Liakhou, R.L. Voti, R.P. Wang, C. Sibilia, A. Syrbu, V. Yakovlev, An experimental and theoretical analysis of the temperature profile in semiconductor laser diodes using the photodeflection technique, Meas. Sci. Technol. 6 (9) (1995) 1278–1290.
[16] J. Bodzenta, Thermal wave methods in investigation of thermal properties of solids, Eur. Phys. J. Spec. Top. 154 (1) (2008) 305–311.
[17] R.M. Costescu, M.A. Wall, D.G. Cahill, Thermal conductance of epitaxial interfaces, Phys. Rev. B 67 (5) (2003) 054302.
[18] A. Koreeda, R. Takano, S. Saikan, Second sound in $SrTiO_3$, Phys. Rev. Lett. 99 (26) (2007) 265502.
[19] Z. Guo, Y. Wan, M. Yang, J. Snaider, K. Zhu, L. Huang, Long-range hot-carrier transport in hybrid perovskites visualized by ultrafast microscopy, Science 356 (6333) (2017) 59–62.
[20] J. Hristov, Steady-state heat conduction in a medium with spatial non-singular fading memory: derivation of Caputo-Fabrizio space-fractional derivative from Cattaneo concept with Jeffrey's kernel and analytical solutions, Therm. Sci. 21 (2) (2017) 827–839.
[21] J. Hristov, Integral solutions to transient nonlinear heat (mass) diffusion with a power-law diffusivity: a semi-infinite medium with fixed boundary conditions, Heat Mass Transf. 52 (3) (2016) 635–655.
[22] C. Cattaneo, Sulla conduzione del calore, Atti del Seminario Fisico Matematico e dell'Università di Modena 3 (1948) 83–101.
[23] P. Vernotte, Paradoxes in the continuous theory of the heat equation, C.R. Bulgarian Acad. Sci. 246 (3) (1958) 153–154.
[24] D.Y. Tzou, The generalized lagging response in small-scale and high-rate heating, Int. J. Heat Mass Transf. 38 (17) (1995) 3231–3240.
[25] R.A. Guyer, J.A. Krumhansl, Solution of the linearized phonon Boltzmann equation, Phys. Rev. 148 (2) (1966) 766–778.
[26] R.A. Guyer, J.A. Krumhansl, Thermal conductivity, second sound, and phonon hydrodynamic phenomena in nonmetallic crystals, Phys. Rev. 148 (2) (1966) 778–788.
[27] Z.Y. Guo, Q.W. Hou, Thermal wave based on the thermomass model, J. Heat Transf. 132 (7) (2010) 072403.
[28] C.C. Ackerman, R.A. Guyer, Temperature pulses in dielectric solids, Ann. Phys. 50 (1) (1968) 128–185.
[29] C.C. Ackerman, B. Bertman, H.A. Fairbank, R.A. Guyer, Second sound in solid helium, Phys. Rev. Lett. 16 (18) (1966) 789–791.
[30] D.W. Pohl, V. Irniger, Observation of second sound in NaF by means of light scattering, Phys. Rev. Lett. 36 (9) (1976) 480–483.
[31] V. Narayanamurti, R. Dynes, Observation of second sound in bismuth, Phys. Rev. Lett. 28 (22) (1972) 1461–1465.
[32] D. Tsai, R. MacDonald, Molecular-dynamical study of second sound in a solid excited by a strong heat pulse, Phys. Rev. B 14 (10) (1976) 4714–4723.
[33] Y.C. Hua, Y. Dong, B.Y. Cao, Monte Carlo simulation of phonon ballistic-diffusive heat conduction in silicon nanofilm, Acta Phys. Sin. 24 (62) (2013) 244401.
[34] D.S. Tang, Y.C. Hua, B.D. Nie, B.Y. Cao, Phonon wave propagation in ballistic-diffusive regime, J. Appl. Phys. 119 (12) (2016) 124301.
[35] D.S. Tang, B.Y. Cao, Ballistic thermal wave propagation along nanowires modeled using phonon Monte Carlo simulations, Appl. Therm. Eng. 117 (2017) 609–616.
[36] M. Al-Nimr, M. Naji, S. Al-Wardat, Overshooting phenomenon in the hyperbolic heat conduction model, Jpn. J. Appl. Phys. 42 (8R) (2003) 5383–5386.
[37] M.T. Xu, J.F. Guo, L.Q. Wang, L. Cheng, Thermal wave interference as the origin of the overshooting phenomenon in dual-phase-lagging heat conduction, Int. J. Therm. Sci. 50 (5) (2011) 825–830.
[38] A. Mandelis, K.F. Leung, Photothermal-wave diffraction and interference in condensed media: experimental evidence in aluminum, J. Opt. Soc. Am. A: 8 (1) (1991) 186–200.
[39] A. Moosaie, G. Atefi, A.A. Fardad, Two-dimensional non-Fourier heat conduction with arbitrary initial and periodic boundary conditions, Forsch. Ingenieurwes. 72 (2) (2008) 67–76.
[40] M. Bertolotti, G. Liakhou, R. Li Voti, S. Paoloni, C. Sibilia, Thermal wave reflection and refraction: Theoretical and experimental evidence, J. Appl. Phys. 85 (7) (1999) 3540–3545.
[41] G.F. Carey, M. Tsai, Hyperbolic heat transfer with reflection, Numer. Heat Transf. Part A: Appl. 5 (3) (1982) 309–327.
[42] J.P. Wu, H.S. Chu, Propagation and reflection of thermal waves in a rectangular plate, Numer. Heat Transf. Part A: Appl. 36 (1) (1999) 51–74.
[43] L. Li, L. Zhou, Y. Zhang, Thermal wave superposition and reflection phenomena during femtosecond laser interaction with thin gold film, Numer. Heat Transf. Part A: Appl. 65 (12) (2014) 1139–1153.
[44] M. Özişik, B. Vick, Propagation and reflection of thermal waves in a finite medium, Int. J. Heat Mass Transf. 27 (10) (1984) 1845–1854.
[45] B. Singh, A. Kumar, J. Singh, Reflection of generalized thermoelastic waves from a solid half-space under hydrostatic initial stress, Appl. Math. Comput. 177 (1) (2006) 170–177.
[46] S.B. Sinha, K.A. Elsibai, Reflection and refraction of thermoelastic waves at an interface of two semi-infinite media with two relaxation times, J. Therm. Stresses 20 (2) (1997) 129–145.
[47] B. Shen, P. Zhang, Notable physical anomalies manifested in non-Fourier heat conduction under the dual-phase-lag model, Int. J. Heat Mass Transf. 51 (7–8) (2008) 1713–1727.
[48] D.Y. Tzou, Reflection and refraction of thermal waves from a surface or an interface between dissimilar materials, Int. J. Heat Mass Transf. 36 (2) (1993) 401–410.
[49] M.K. Zhang, B.Y. Cao, Y.C. Guo, Numerical studies on dispersion of thermal waves, Int. J. Heat Mass Transf. 67 (2013) 1072–1082.
[50] J.R. Ho, C.P. Kuo, W.S. Jiaung, Study of heat transfer in multilayered structure within the framework of dual-phase-lag heat conduction model using lattice Boltzmann method, Int. J. Heat Mass Transf. 46 (1) (2003) 55–69.
[51] J. Ordóñez-Miranda, J.J. Alvarado-Gil, Effective thermal properties of multilayered systems with interface thermal resistance in a hyperbolic heat transfer model, Int. J. Thermophys. 31 (4–5) (2010) 900–925.
[52] K. Ramadan, Semi-analytical solutions for the dual-phase-lag heat conduction in multilayered media, Int. J. Therm. Sci. 48 (1) (2009) 14–25.
[53] K. Ramadan, M. Al-Nimr, Analysis of the thermal behavior of a multilayer slab with imperfect contact using the dual-phase-lag heat conduction model, J. Heat Transf. 130 (7) (2008) 074501.
[54] K. Ramadan, M. Al-Nimr, Analysis of transient heat transfer in multilayer thin films with nonlinear thermal boundary resistance, Int. J. Therm. Sci. 48 (9) (2009) 1718–1727.
[55] M. Al-Nimr, M. Naji, R. Abdallah, Thermal behavior of a multi-layered thin slab carrying periodic signals under the effect of the dual-phase-lag heat conduction model, Int. J. Thermophys. 25 (3) (2004) 949–966.
[56] B.C. Li, S.Y. Zhang, The effect of interface resistances on thermal wave propagation in multi-layered samples, J. Phys. D Appl. Phys. 30 (10) (1997) 1447–1454.
[57] T. Niu, W. Dai, A hyperbolic two-step model based finite difference scheme for studying thermal deformation in a double-layered thin film exposed to ultrashort-pulsed lasers, Int. J. Therm. Sci. 48 (1) (2009) 34–49.
[58] H. Wang, W. Dai, L.G. Hewavitharana, A finite difference method for studying thermal deformation in a double-layered thin film with imperfect interfacial contact exposed to ultrashort pulsed lasers, Int. J. Therm. Sci. 47 (1) (2008) 7–24.
[59] N.S. Al-Huniti, M. Al-Nimr, Thermoelastic behavior of a composite slab under a rapid dual-phase-lag heating, J. Therm. Stresses 27 (7) (2004) 607–623.
[60] A. Khadrawi, M. Al-Nimr, M. Hammad, Thermal behavior of perfect and imperfect contact composite slabs under the effect of the hyperbolic heat conduction model, Int. J. Thermophys. 23 (2) (2002) 581–598.
[61] W.B. Lor, H.S. Chu, Propagation of thermal waves in a composite medium with interface thermal boundary resistance, Numer. Heat Transf. Part A: Appl. 36 (7) (1999) 681–697.
[62] W.B. Lor, H.S. Chu, Effect of interface thermal resistance on heat transfer in a composite medium using the thermal wave model, Int. J. Heat Mass Transf. 43 (5) (2000) 653–663.
[63] K.C. Liu, Analysis of thermal behavior in multi-layer metal thin films based on hyperbolic two-step model, Int. J. Heat Mass Transf. 50 (7–8) (2007) 1397–1407.
[64] Y.C. Hua, B.Y. Cao, Phonon ballistic-diffusive heat conduction in silicon nanofilms by Monte Carlo simulations, Int. J. Heat Mass Transf. 78 (2014) 755–759.
[65] Y.C. Hua, B.Y. Cao, Slip boundary conditions in ballistic–diffusive heat transport in nanostructures, Nanoscale Microscale Thermophys. Eng. 21 (3) (2017) 159–176.
[66] D.Y. Tzou, J.C. Dowell, Computational techniques for microscale heat transfer, second ed., Handbook of Numerical Heat Transfer, 2006, pp. 623–657.
[67] A. Salazar, Energy propagation of thermal waves, Eur. J. Phys. 27 (6) (2006) 1349–1355.
[68] B.S. Hong, P.J. Su, C.Y. Chou, C.I. Hung, Realization of non-Fourier phenomena in heat transfer with 2D transfer function, Appl. Math. Model. 35 (8) (2011) 4031–4043.
[69] M.K. Zhang, B.Y. Cao, Y.C. Guo, Numerical studies on damping of thermal waves, Int. J. Therm. Sci. 84 (2014) 9–20.
[70] D. Zhang, A course in Computational Fluid Dynamics, China Higher Education Press, Beijing, 2010, pp. 185–189.
[71] B.H. Bai, Authoritative Guide on Fortran Program Designing, China Machine Press, Beijing, 2013, pp. 415–418.
[72] J.H. Choi, S.H. Yoon, S.G. Park, S.H. Choi, Analytical solution of the Cattaneo-Vernotte equation (non-Fourier heat conduction), J. Kor. Soc. Mar. Eng. 40 (5) (2016) 389–396.